Automatic geolocation and measuring of offshore energy infrastructure with multimodal satellite data.

MA, P., MACDONALD, M., ROUSE, S. and REN, J.

2024

Automatic Geolocation and Measuring of Offshore Energy Infrastructure With Multimodal Satellite Data

Ping Ma ⓘ, Malcolm Macdonald ⓘ, Sally Rouse ⓘ, and Jinchang Ren ⓘ, *Senior Member, IEEE*

Abstract—With the increasing trend of energy transition to low-carbon economies, the rate of offshore structure installation and removal will rapidly accelerate through offshore renewable energy development and oil and gas decommissioning. Knowledge of the location and size of offshore infrastructure is vital in the management of marine ecosystems and also for safe navigation at sea. The availability of multimodal data enables the systematic assessment of offshore infrastructure. In this article, we propose an automatic solution for the geolocation and size evaluation of offshore infrastructure through a data fusion model of Sentinel-1 synthetic aperture radar (SAR) data and Sentinel-2 multispectral instrument imagery. The use of the Sentinel-1 (SAR) data aims to quickly localize candidate offshore energy infrastructure with its all-weather imaging capabilities, while the high-resolution optical data provided by the Sentinel-2 can enable more accurate localization and measurement of the offshore infrastructure. To be specific, a candidate detection model is applied to a time series of Sentinel-1 images to extract the "guided area" of the infrastructure, followed by morphological operation-based precise localization within an individual Sentinel-2 image, as well as estimating the size of each structure. With validation against the ground truth data of the Scottish waters from the baseline and closing bays, to the limit of the exclusive economic zone of Scotland, an area of 371 915 km^2, our method has automatically identified 332 objects with an omission error of 0.3% and a commission rate of 0%. Our method was comprehensively compared with two state-of-the-art offshore energy infrastructure detection algorithms. The results validate that our method achieves the highest overall accuracy of 99.70%, surpassing the compared ones by 3.84%–12.50%. For the size evaluation, the achieved mean errors of the topside area size of oil/gas platforms and diameter length measurement of wind turbines both are 1 pixel in Sentinel-2 images, providing an effective technique for the identification and estimation of offshore infrastructure.

Ping Ma and Jinchang Ren are with the National Subsea Centre, Robert Gordon University, AB21 0BH Aberdeen, U.K. (e-mail: p.ma.strath@gmail.com; jinchang.ren@ieee.org).
Malcolm Macdonald is with the Applied Space Technology Laboratory, Centre for Signal and Image Processing, Department of Electronic and Electrical Engineering, University of Strathclyde, G1 1XW Glasgow, U.K. (e-mail: malcolm.macdonald.102@strath.ac.uk).
Sally Rouse is with the Offshore Energy Environmental Advice Group, Marine Scotland Science, AB11 9DB Aberdeen, U.K. (e-mail: sally.rouse@gov.scot).

Index Terms—Multimodal satellite data, offshore oil/gas platforms, offshore wind turbines, size assessment.

I. INTRODUCTION

THE introduction of engineered structures to the marine environment can have profound effects on the ecosystems, including through interactions with oceanographic processes, biological productivity, and the spatial distribution of fish, mammals, and birds [1], [2]. Authorities, in different countries, such as the global marine science community, governments/regulators, and operators are actively seeking greater international alignment on installation and removal practices as well as policies for offshore infrastructure to ensure their impacts on the marine environment are minimized. This requires accurate and accessible knowledge of structures, especially their quantity, spatial distribution, and size.

Globally, energy infrastructure, including oil and gas platforms, and wind turbines constitute a substantial proportion of offshore structures [3], [4]. Many countries maintain databases of offshore energy structures. However, many of these databases have restricted access, inaccurate data, omissions, and/or lack of up-to-date information [5], [6]. Moreover, oil and gas production platforms can be relocated, creating a risk to the safe navigation of shipping if nautical charts are not promptly updated with new location data. Thus, it is highly demanding to develop a method to quickly and accurately detect the location and properties (e.g., size, shape, type, structural details) of offshore infrastructure. Although there are many conventional survey approaches that can provide highly accurate detection, they are generally unsuitable for deployment at the global scale because of the high degree of time and cost requirements [7]. With the advancement of space-based remote sensing technologies, a wide range of satellite data is now being acquired from diverse sensors, leading to the emergence of multimodal satellite data. As different modalities of data may provide supplementary information to each other, such as various coverage and imaging conditions, the combination of them can help to achieve more robust and accurate detection and measurements [8]. These data have the capabilities of short revisit periods, low cost, and synchronous observations in larger areas [9], [10]. Synchronous observation refers to the capability of satellites to capture the data simultaneously or nearly simultaneously over a large area [11], [12]. Such capabilities will allow for the timely identification and understanding of the dynamic changes in the large observed area,

offering great potential for efficient and effective monitoring of the offshore energy infrastructure.

For the observation of offshore energy infrastructure, satellites offer a frequently updated, and archived, near-global database. For example, Liu et al. [7] proposed an automatic method with the Landsat-8 operational land imager (OLI) (band 6) for the detection of offshore platforms in the Persian Gulf, the Gulf of Mexico, and the Gulf of Thailand. This method considers the features of spectra, texture, size, location, and shape to discriminate the platforms from the ocean background. In [13], offshore oil/gas platforms in the South China Sea are identified using Landsat optical images, using multiple sliding windows with dynamic thresholds to recognize candidate objects. Followed by laminating, three images of consecutive periods are combined or layered to label interested objects, e.g., oil/gas platforms only when their presence is confirmed in all three images. To improve the platform detection accuracy with a single image, Zhu et al. [14] employed the Harris detector and intensity-texture feature image to extract the platforms from a Sentinel-2 L2A Image in the Persian Gulf of Mexico area. Xu et al. [15] developed a visual saliency detection approach to determine the status of offshore wind turbines in the North Sea and surrounding waters, based on the time series of multisource optical satellite images, including Landsat-5 thematic mapper (TM), Landsat-7 thematic mapper plus (ETM+), Landsat-8 OLI), and Sentinel-2 multispectral instrument (MSI). Zhu et al. [16] proposed an automatic method for offshore platform identification on the Landsat 7 ETM+ images in the Caspian Sea area, where a cloud shadow-free normalized difference water index (NDWI) composite was built with multiple threshold segmentations to remove the influence of cloud and extract drilling rigs. Strikingly, all these methods employed optical imagery and so suffered from cloud contamination, which can significantly reduce the number of available images for object detection.

The high temperature and the brightness of waste gas flames at night have also been used for the identification and monitoring of oil and gas platforms. Croft [17] first used the DMSP/OLS night-time light image data to identify the waste gas flame. Casadio et al. [18] monitored the night-time gas flaring activity of the extracted offshore oil/gas platforms in the North Sea area through the fusion of the synthetic aperture radar (SAR) and along track scanning radiometer (ATSR) data. The positions of rigs are first extracted by SAR data, and then flaring activity is estimated on the short-wave infrared (SWIR) band (1.6 μm) at ATSR. Anejionu et al. [19] developed a double threshold segmentation approach for the retrieval of the flaring location and the volume of gas combusted in the Niger Delta from 2000 to 2014 through nighttime moderate-resolution imaging spectroradiometer thermal imagery. Elvidge et al. [20] further refined the network function virtualization algorithm [21] to extract global waste gas combustion sources based on the thermal anomalies with high-resolution national polar-orbiting operational environmental satellite system preparatory project/visible infrared imaging radiometer images. Some, but not all, of these methods resolve the issue of cloud contamination; however, they are only applicable to platforms with gas combustion, and therefore not able to detect the full suite of energy infrastructure in the marine environment.

Given the capability of imaging through cloud and in darkness, SAR can overcome the shortcomings of optical imagery. For example, Cheng et al. [22] extracted offshore oil/gas platforms from multitemporal ENVISAT ASAR data by a two-parameter constant false alarm rate (CFAR) detector. Wong et al. [6] detected offshore infrastructure, including oil platforms or platform complexes and wind turbines, by using multitemporal SAR and Google Earth Engine (GEE), in which the median composite, Gaussian difference, thresholding, and morphological postprocessing are adopted. An et al. [23] proposed an iterative cell averaging CFAR method to detect offshore wind turbines and oil rigs by monitoring the stationariness of marine targets on strict time series of GF-3 and RADARSAT-2 SAR data. Nunziata et al. [24] developed a dual-polarimetric model utilizing X-band COSMO-SkyMed PingPong mode SAR data for metallic target observation, employing a correlation-based approach and a CFAR method. Xu et al. [25] introduced a machine learning-based approach for dynamic detection of offshore wind turbines from Sentinel-1 SAR data, which includes a cumulatively averaging operator, a refined Lee filter and CFAR technique for noise reduction, a random forest model trained on the GEE platform, and mathematical morphology-based spatial data differentiation for monitoring wind turbine changes, demonstrating high accuracy and potential for global offshore wind turbine detection. Liu et al. [26] presented a time-series remote sensing approach for detecting offshore oil/gas platforms on multisource optical and SAR images. The method employed a stepwise optimization strategy to mitigate noise and a cross-geocorrection strategy using high-geometric accuracy images to rectify poorly georeferenced images. Marino et al. [27] proposed a multipolarization model to analyze the backscattering behavior of offshore platforms using dual-polarization X-band SAR imagery, aiming to address the challenge of reduced copolarized backscattered intensity under low incidence angles. Liu et al. [28] developed a novel method for the detection of global offshore oil/gas platforms by using the position-invariant characteristic, which aims to systematically evaluate the geometric location accuracy of medium-resolution remote sensing data on ocean scenes. This study validated that the data from the Sentinel-1, Sentinel-2, ENVISAT, and ALOS-1 have higher geometric accuracy than those from the JERS-1 and RADARDAT-1. Zhang et al. [3] created a global offshore wind turbine database using the Sentinel-1 SAR time-series images spanning from 2015 to 2019. Through the utilization of a percentile-based annual SAR image reduction and autoadaptive thresholding algorithm implemented on the GEE platform, the geolocations of worldwide offshore wind turbines are successfully identified. Hoeser et al. [29] introduced the deep-learning-derived offshore wind turbines data set, a global-scale open-access data set utilizing Sentinel-1 SAR data, along with deep-learning-based object detection using two cascading convolutional neural networks. This data set provides information on the deployment stages of offshore wind energy infrastructure with a quarterly frequency spanning from July 2016 to June 2021.

Although these studies have presented ways for geolocating offshore energy infrastructure, most of them fail to offer a more detailed analysis in terms of accurate location and size measurement of different types of infrastructure. In this article, an automatic geolocating and measuring approach to offshore energy infrastructure is proposed by combining the strengths of both the Sentinel-1 SAR and Sentinel-2 MSI images. To quickly geolocate the offshore energy infrastructure, the inherent capacity of SAR to mitigate the impact of adverse weather conditions is utilized. The time-series Sentinel-1 data in conjunction with temporal background modeling and 2-D-singular spectrum analysis (SSA) filtering are employed to first detect the candidate regions of interest as potential objects, referred to as "guided area." The geolocation is then further refined by employing the proposed spectral-spatial method, namely, RGB (red (R), green (G), and blue (B) bands) fused morphological reconstruction on the Sentinel-2 MSI data. To measure the offshore energy infrastructure, a size estimation model is subsequently introduced. Specifically, a novel classification method is introduced, leveraging spatial characteristics, to automate the classification of offshore energy infrastructure. Finally, the topside area of the oil/gas platform and the diameter length of the wind turbine are measured. This proposed framework is validated against a ground truth data set of the whole Scottish waters, covering an area of $371\,195\,\text{km}^2$. The major contributions of this article can be summarized as follows.

1) We present the first attempt to fuse the Sentinel-1 and Sentinel-2 data for geolocating offshore energy infrastructures. By harnessing the complementary strengths of the SAR and MSI data, our approach achieves efficient and accurate geolocation of offshore energy infrastructures, including the identification of diverse rigs within interconnected oil/gas platforms, which are typically treated as a single entity in most existing studies. This work increases the necessary granularity in geolocation analysis for oil/gas platforms.

2) It is also the first time for the automated size measurement of offshore energy infrastructure from satellite data. The diameter length of the wind turbines and the topside area size of the oil/gas platforms and semipermanent objects are measured independently. The proposed automatic geolocation and size measurement provides a comprehensive understanding of the offshore energy infrastructure landscape.

3) A novel classification method is presented to effectively distinguish wind turbines from other types of offshore energy infrastructure. The proposed method offers an automated pathway for the subsequent monitoring and measurement of offshore energy infrastructures, providing a streamlined approach to these crucial tasks.

II. STUDY AREAS AND DATA SETS

A. Study Areas

The study area covers Scotland's exclusive economic zone (EEZ) and the baseline of the United Kingdom (U.K.) as well as the closing bays (see Fig. 1). Note that the infrastructure within internal waters is excluded because of the practice of "parking"
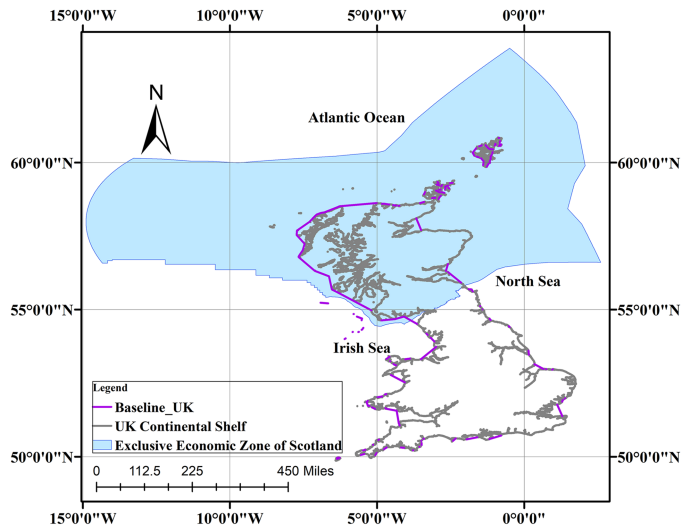
Fig. 1. Scottish EEZ: Location of the study area.

oil and gas platforms within internal waters for variable periods and the corresponding challenge of generating accurate ground-truth data. Most of the infrastructure is located beyond the baseline and future energy structures are likely to be constructed further offshore [30]. Scotland is located in northwest Europe and surrounded by the North Sea on the east, the North Channel and the Irish Sea on the southwest, and the Atlantic Ocean on the north and west. The water depths of the study area vary from shallow coastal waters to more than 2000 m in some ocean areas. Scottish waters cover approximately $371\,915\,\text{km}^2$ and contain some of the largest oil reserves in Europe. Offshore hydrocarbon exploitation began in the 1970s and remains a major but declining activity in Scottish waters. Typical oil and gas installations within Scottish waters include platforms that are either concrete gravity-based or fixed steel jackets. Fixed steel jackets can comprise a single integrated platform or bridge-linked two or more platforms, which inevitably increases the difficulty of platform identification in satellite imagery. In recent years, the Scottish government has promoted offshore renewable energy. Several offshore wind farms have been constructed, including Beatrice Offshore Wind Farm, Moray East Offshore Wind Farm (under construction), HyWind Offshore Wind Farm (Aberdeenshire), Kincardine Offshore Wind Farm (Aberdeenshire), and Aberdeen Offshore Wind Farm (Aberdeen Bay). The Beatrice Offshore Wind Farm with wind turbines located 25 km from the Scottish shoreline was the world's deepest offshore wind project at the time of construction. The Scottish waters also host various semipermanent objects, i.e., the structures or installations that are intended to remain in place for an extended period of time but are not permanent fixtures. These objects serve specific purposes and can be moved or relocated as needed. Examples of semipermanent objects include floating production storage and offloading (FPSO) vessels and floating storage units.

B. Data Sets

The data used in this study include images and auxiliary data. Image data are employed to identify offshore energy

infrastructure in Scottish waters and analyze their sizes. Auxiliary data are used to assemble the ground truth data set and validate the spatial distribution and size of offshore infrastructure and performance evaluation.

1) Ground Truth Data Set: In this article, a ground truth data set of offshore energy infrastructures is constructed using:
1) Scottish Waters (200M Limit) - EEZ [30];
2) the Scotland coastline and baseline [31];
3) the Oslo and Paris Commissions Inventory of Offshore Installations-2019 [32];
4) the offshore infrastructure distributions on the U.K.'s Continental Shelf provided by the Oil and Gas Authority [33];
5) the actual topside area size of oil/gas platforms measured by experts' knowledge and measurement tools, which are available in the EO Browser interface [34];
6) the Beatrice Offshore Wind Farm consent plan [35];
7) development layout and specification plan for Moray East Offshore Wind Farm [36];
8) the Design Statement for Aberdeen Offshore Wind Farm [37];
9) the Construction Plan for Hywind Wind Farm [38];
10) Kincardine Offshore Wind Farm Environmental Scoping Assessment [39].

The summarized ground truth data are given in Supplementary Material (see Tables S1–S6).

2) Images for the Proposed Method: The satellite data used in this study include the Sentinel-1 SAR data and Sentinel-2 MSI data.

Sentinel-1, developed by the European Space Agency (ESA) as part of the Copernicus program, is a constellation of two radar imaging satellites: Sentinel-1A and Sentinel-1B. Launched on 3 April 2014 and 25 April 2016, respectively, these satellites are equipped with a SAR instrument, which operates in the C-band frequency range, enabling the measurement of the backscatter signals reflected from the Earth's surface. The repeat cycle for a single Sentinel-1 satellite is 12 days, while a combined operation of the Sentinel-1A and Sentinel-1B satellites is used to ensure a revisit cycle of 6 days [40], [41]. SAR images acquired by the Sentinel-1 encapsulate both coherent, signifying interferometric phases, and incoherent, pertaining to the amplitude features, components of information. Sentinel-1 offers several imaging modes to cater to diverse user needs. These include the stripmap, interferometric wide swath (IW), extra wide swath, and Wave modes. The IW mode is particularly valuable for large-scale monitoring and mapping activities. It captures the SAR images with a swath width of up to 250 km and achieves a spatial resolution of 5×20 m. In addition, the IW mode provides valuable dual-polarization data, including the vertical transmit and vertical receive (VV) and the vertical transmit and horizontal receive (VH) polarization. The orthorectified VH Sentinel-1 data can be achieved using preprocessing steps, including radiometric calibration, thermal noise removal, speckle filter, geometric correction, orthorectification, and terrain correction.

The Sentinel-2 data were also acquired from the ESA, which operates as part of the Copernicus program. The Sentinel-2A (launched on 23 June 2015) and 2B (launched on 7 March 2017) satellites offer a combined revisit period of five days and possess a wide swath width of 290 km. Both Sentinel-2A and Sentinel-2B satellites are equipped with a single MSI that captures imagery across 13 spectral bands. These bands include visible, near-infrared, and SWIR bands with a spatial resolution of 10 m, 20 m, and 60 m, respectively. The Sentinel-2 data can be processed to obtain higher level surface reflectance products (Level-2A) by transforming the top-of-atmosphere reflectance product (Level-1C) using atmospheric correction techniques. In this study, the bands in blue (Band #2), green (Band #3), and red (Band #4) of Sentinel-2 Level-2A data are used.

The main advantage of the Sentinel-1 data lies in its ability to provide all-weather and day-and-night imaging capabilities through the use of SAR technology, overcoming the limitations of cloud cover in Sentinel-2 level 2A data. On the other hand, Sentinel-2 level 2A data, with its optical imaging capabilities, offer higher spatial resolution and richer spectral information. This facilitates the observation of intricate details on the Earth's surface, such as small-sized infrastructure and complex oil/gas structures.

In this article, we selectively downloaded 95 orthorectified VH Sentinel-1 images, covering the period from June 2020 to February 2022 and 33 Sentinel-2 Level 2A data with RGB bands spanning from March 2020 to February 2022 from the EO browser [34]. The software and metadata used to generate the results in this article are provided by DOI of 10.5281/zenodo.8171739.

III. METHODOLOGY

The proposed method includes two schemes: location detection and size estimation. Fig. 2 shows the workflow of the framework. First, the Sentinel-1 time-series data are processed through three strategies to detect the "guided area," or estimated contour position of the candidate offshore infrastructures. Then, this "guided area" is used to quickly locate the offshore candidates in locally cloud-free Sentinel-2 data. Finally, three steps are employed based on clear shape and structural information on Sentinel-2 to refine the location and estimate the size of each structure.

A. Data Fusion Model for Geolocation of Interested Objects

1) Candidate Detection From Sentinel-1 Time-Series Data:

a) Temporal analysis for modeling of background targets: The ocean surface is a dynamic environment. There are a variety of moving objects and changing wakes generated in the surrounding water of offshore infrastructure. However, oil/gas platforms and wind turbines have a temporally invariant position. For detecting these offshore infrastructures, it is essential to design an effective background model by removing moving, short-duration, or subtly shifting objects. In general, the running average and mixed Gaussian model are widely used for modeling the background [7], [16]. However, the running average method is easily affected by the noises in a monophase image. The Gaussian model requires high computational cost. In this article, a simple and fast method, namely, a temporal median-filtered approach [28], is applied.
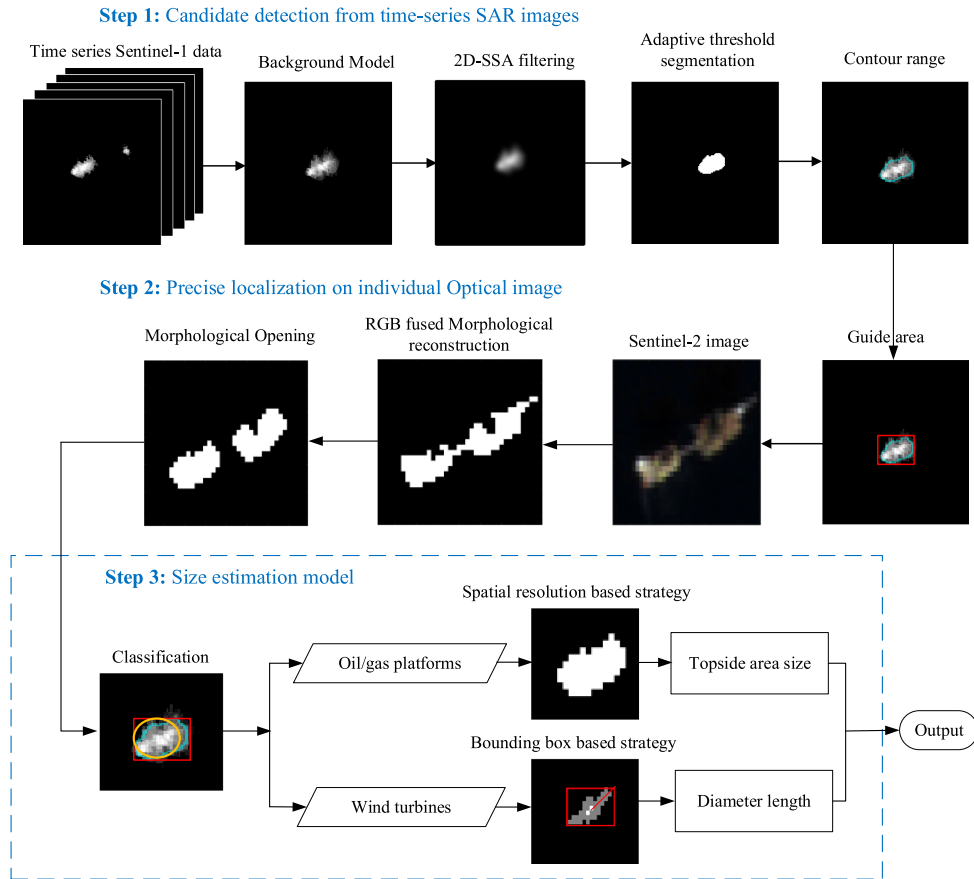
Fig. 2. Flowchart of the proposed method.
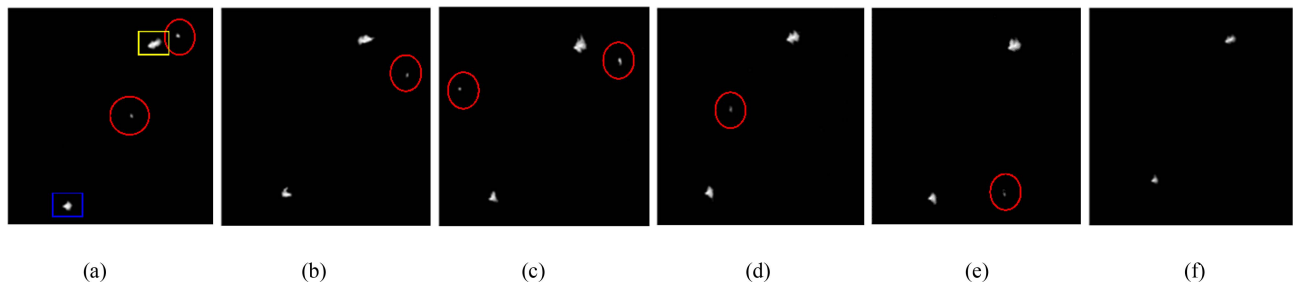
Fig. 3. Platform Clair (marked in blue rectangle) and the linked platform consisting of Clair ridge drilling and process (DP) and Clair ridge quarters and utilities (QU) (marked in yellow rectangle), and false positives (vessels and noise, marked in red circles) in the Sentinel-1 data. (a) Data ID: 2020-06-20-00_00_2020-06-20-23_59_Sentinel-1_AWS-IW-VVVH_VH_-_decibel_gamma0_-_orthorectified. (b) Data ID: 2020-08-19-00_00_2020-08-19-23_59_Sentinel-1_AWS-IW-VVVH_VH_-_decibel_gamma0_-_orthorectified. (c) Data ID: 2020-10-18-00_00_2020-10-18-23_59_Sentinel-1_AWS-IW-VVVH_VH_-_decibel_gamma0_-_orthorectified. (d) Data ID: 2020-12-17-00_00_2020-12-17-23_59_Sentinel-1_AWS-IW-VVVH_VH_-_decibel_gamma0_-_orthorectified. (e) Data ID: 2021-02-15-00_00_2021-02-15-23_59_Sentinel-1_AWS-IW-VVVH_VH_-_decibel_gamma0_-_orthorectified. (f) Temporal median image of five time-series images.

The SAR time-series data are adopted to model background targets by using temporal changes. For each scene, the Sentinel-1 time-series images are employed. The median intensity value of each pixel from time-series images is calculated as follows:

$$I^M(x, y) = \text{median}\{I_n(x, y)\} \quad n = 1, 2, \ldots, N \quad (1)$$

where (x, y) is the pixel location, I_n is the nth image in the time series, N denotes the total number of time-series images, and I^M is the median image, i.e., the estimated static background. To balance between the detection accuracy and computational efficiency, N is set to 5 in this study. Among time-series images, the oil/gas platforms and wind turbines have a higher occurrence frequency than the moving objects. As a result, on the temporal median-filtered image, due to low occurrence frequency, the vessels and speckle noises can be successfully removed.

As shown in Fig. 3(a)–(e), different vessels (marked in red circles) appear on the Sentinel-1 data on different dates, while there are ships close to the oil/gas platforms. This will inevitably increase the difficulty of removing them from the images. Using the subtle position changes, the temporal median operation has successfully filtered these ships and reduced the noise as depicted in Fig. 3(f). Overall, the background ocean noise is

This article has been accepted for inclusion in a future issue of this journal.

IEEE JOURNAL OF OCEANIC ENGINEERING
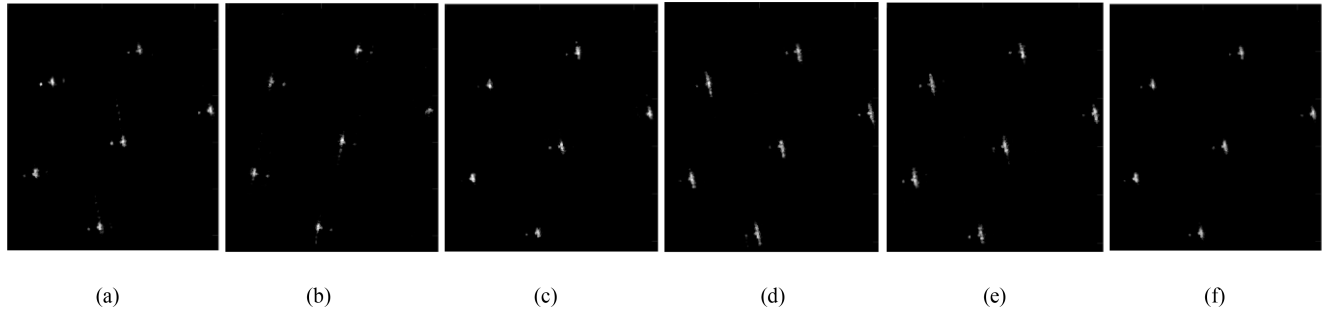
Fig. 4. Five Sentinel-1 SAR images of the offshore wind turbines in the Beatrice Wind Farm. (a) Data ID: 2020-06-20-00_00_2020-06-20-23_59_Sentinel-1_AWS-IW-VVVH_VH_-_decibel_gamma0_-_orthorectified. (b) Data ID: 2020-08-19-00_00_2020-08-19-23_59_Sentinel-1_AWS-IW-VVVH_VH_-_decibel_gamma0_-_orthorectified. (c) Data ID: 2020-10-18-00_00_2020-10-18-23_59_Sentinel-1_AWS-IW-VVVH_VH_-_decibel_gamma0_-_orthorectified. (d) Data ID: 2020-12-17-00_00_2020-12-17-23_59_Sentinel-1_AWS-IW-VVVH_VH_-_decibel_gamma0_-_orthorectified. (e) Data ID: 2021-02-15-00_00_2021-02-15-23_59_Sentinel-1_AWS-IW-VVVH_VH_-_decibel_gamma0_-_orthorectified. (f) Result of temporal median image.

suppressed, yet the offshore infrastructure is accentuated. Similar results are also obtained for the wind farm areas. It is clear from Fig. 4(a)–(e) that, as expected, the blade part of the wind turbine changes direction over time. By considering the wind turbine on different dates via the temporal median operation, the main structures of these rotating objects are maintained with the background noise removed.

b) 2D-SSA filtering for smoothing the images: The temporal median operation can minimize the noisy objects from moving objects in the background. However, there is still other noise remaining, especially the water wake around the offshore infrastructure, which can affect the geolocation accuracy [42]. To filter such noise on the edges of infrastructure while keeping more details and clear contours, the 2D-SSA method is employed, which is an effective and noise-robust spatial feature extraction tool [43], [44]. For a grayscale image, the 2D-SSA method can decompose the image into several components and reconstruct a new image with the main information and spatial structures. For the image I^M with size of $N_x \times N_y$, a sliding window L with size of $L_x \times L_y$, where $L_x \in [1, N_x]$ and $L_y \in [1, N_y]$, is defined. Then, a trajectory matrix $X \in R^{L \times K}$ can be generated, where $K = (N_x - L_x + 1)(N_y - L_y + 1)$. The matrix X exhibits a structure called the Hankel-block-Hankel (HbH), which is Hankel in block terms with each one of the blocks being Hankel by itself [43]. The matrix X is decomposed by the singular value decomposition, resulting in eigenvalues and corresponding eigenvectors. Afterward, the eigenvalue grouping is carried out, wherein multiple components are chosen to form a new matrix X_t through grouping. Note that the resulting matrix X_t is not necessarily the HbH type. To transform X_t into HbH matrices, a two-step Hankelization operation is used, which involves first applying an averaging procedure within each block and subsequently applying it between the blocks. Finally, the reconstructed final image I^{Re} is obtained. Details description of the 2D-SSA process can be found in [43] and [45]. In this article, the number of components N_c and the size of the filtering window in 2D-SSA are set to 1 and 5×5, respectively. The determination of these parameters is illustrated in Supplementary Material (see Figs. S1 and S2).

c) Adaptive threshold segmentation for object detection: After obtaining a filtered image, an adaptive threshold segmentation is applied to extract the candidate regions of interest as potential objects. The widely used method, OTSU [46], is employed here to adaptively determine an optimal threshold for each scene by maximizing the weighted sum of between-class variance of the foreground and the background. Specifically, OTSU is first applied to obtain the threshold value T_{S1}. Pixels with intensity values higher than T_{S1} are considered for offshore infrastructure as follows:

$$\text{OD}_{s1}(x, y) = \begin{cases} 1, & \text{if } I^{Re} > T_{S1} \\ 0, & \text{otherwise} \end{cases}. \quad (2)$$

As seen in Fig. 5(a) and (f), there is a lots of noise remaining in the temporal median image, especially on the edges of the object. We can find from Fig. 5(c) and (h) that the 2D-SSA filter can effectively smoothen the temporal median image, especially on the edge area. When applying the threshold segmentation, the detection results in Fig. 5(b) and (g) show many noises on the edges, even on the ocean background (marked with a red circle). In contrast, the segmentation on the 2D-SSA-filtered image, as shown in Fig. 5(d) and (i), presents better performance. Based on the detection result in Fig. 5(d) and (i), the contour range can be acquired, as shown in Fig. 5(e) and (j). From Fig. 5, for different kinds of offshore infrastructures with varying characteristics, the OTSU method exhibits effective performance in selecting a proper threshold to extract the contour ranges. However, because of the low spatial resolution, it is difficult to detect the location of each platform from the linked platform's structure, as shown in Fig. 5(a)–(e), i.e., the linked platforms are identified as one object. This problem will further be addressed by combining Sentinel-1 with the high-resolution Sentinel-2 data in the following section.

2) Precise Localization on Individual Sentinel-2 Data: Without the effect of clouds, the Sentinel-1 data can efficiently obtain the approximate locations of offshore infrastructure. Then, the high-resolution Sentinel-2 data are further applied for precise localization. As shown in Fig. 6(a) and (b), the detected object from Sentinel-1 has indicated a larger size than that from the Sentinel-2 image, mainly because of the wake detected around the oil/gas platforms in the Sentinel-1 data. The SAR sensor in Sentinel-1 is particularly sensitive to surface roughness and can capture the wakes created by moving vessels or oil/gas platforms on the water [47]. In contrast, Sentinel-2 is equipped with a multispectral optical sensor and focuses on land monitoring [48]. The wakes are invisible or nondistinguishable in Sentinel-2 images, as shown in Fig. 6(b). Given this, the

This article has been accepted for inclusion in a future issue of this journal.

MA et al.: AUTOMATIC GEOLOCATION AND MEASURING OF OFFSHORE ENERGY INFRASTRUCTURE WITH MULTIMODAL SATELLITE DATA
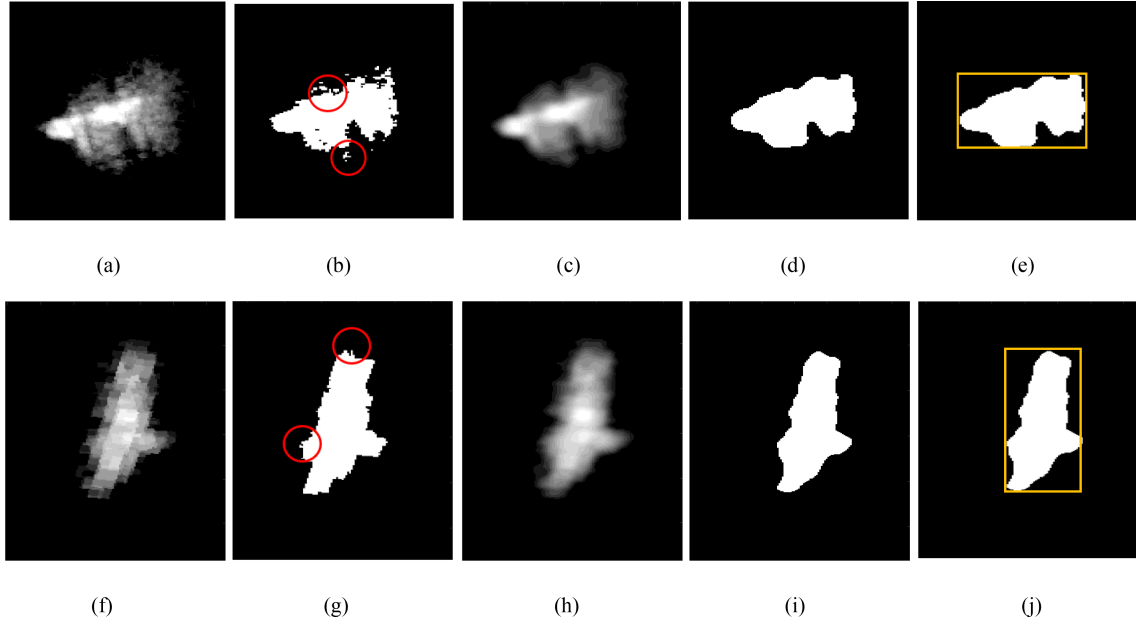
Fig. 5. 2D-SSA filtering and threshold segmentation results. (a) Temporal median image of the linked platforms Clair ridge DP and Clair ridge QU. (b) Threshold segmentation results on (a). (c) 2D-SSA filtered image of (a). (d) Threshold segmentation results on (c). (e) Detected contour range on (d). (f) Temporal median image of the wind turbine BE-A5. (g) Threshold segmentation results on (f). (h) 2D-SSA filtered image of (f). (i) Threshold segmentation results on (h). (j) Detected contour range on (i).
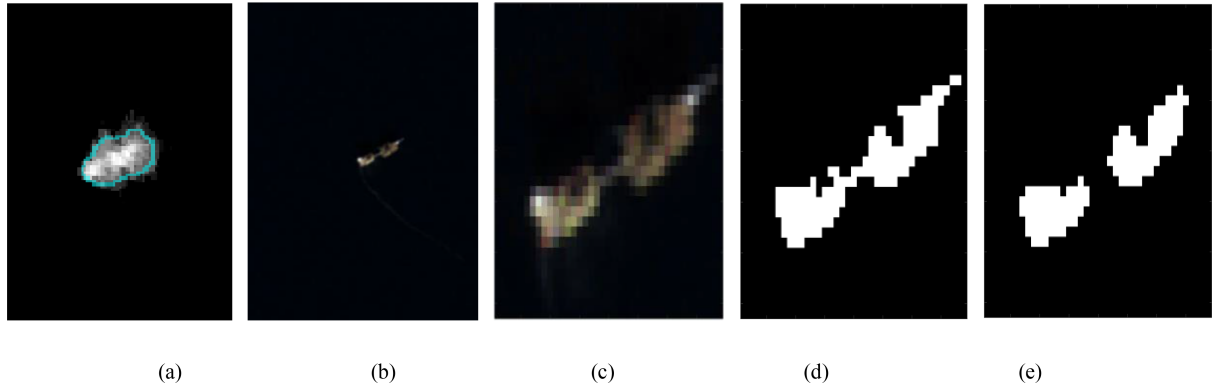
Fig. 6. Platform identification from the linked structure of Clair ridge DP and Clair ridge QU. (a) Linked structure in Sentinel-1 data with the contour range marked in cyan. (b) Linked structure in the Sentinel-2 true color image covered the same latitude and longitude range of (a). (c) Zoomed-in image of (b) in "guided area" (contour range). (d) Detection result OD_f using RGB fused morphological reconstruction. (f) Detection result after the adaptive morphological opening operator.

detected contour range on Sentinel-1 data in Section III-A1 is taken as a "guided area" to refine the precise detection of the offshore infrastructures using the Sentinel-2 data, especially for the separation of the linked structures. In this section, a spectral-spatial detection method, namely, RGB fused morphological reconstruction is proposed.

The morphological reconstruction can extract spatial features by fully utilizing the shape and size information of objects from the input image. Given the different distinguishability of red, green, and blue bands in the Sentinel-2 image, the morphological reconstruction is separately performed on the R, G, and B channels. First, the opening-by-reconstruct operation is applied as follows:

$$O_R = \vee_{k \geq 1} D_{I_R}^{(k)} (I_R \ominus b) \tag{3}$$

where I_R is the R channel in Sentinel-2, b is the structural element, and $(I_R \ominus b)$ is the erosion of I_R by b. Here, a disc

structural element is employed because it satisfies the rotation invariance, and thus can avoid causing potential distortion of image features [49]. The radius size of b is set to 2. The grayscale reconstruction $D_{I_R}(I_R \ominus b)$ is operated by iterating grayscale geodesic dilations for k times until stability is reached. In each iteration, it is calculated as follows:

$$D_{I_R}^{(1)} (I_R \ominus b) = [(I_R \ominus b) \oplus b] \wedge I_R \tag{4}$$

where $\oplus$ stands for the dilation and $\wedge$ presents the pointwise minimum.

Then, a closing-by-reconstruction is used to refine the shape

$$C_R = \vee_{k \geq 1} E_{O_R}^{(k)} (O_R \oplus b) \tag{5}$$

$$E_{O_R}^{(1)} (O_R \oplus b) = [(O_R \oplus b) \ominus b] \vee O_R \tag{6}$$

where $\vee$ stands for the pointwise maximum.

In morphological reconstruction, the erosion and dilation can significantly remove irregular noises on the object surface, while the pointwise computation with input image maintains the shape details of objects. Finally, a threshold also using OTSU is obtained, T_{S2}, to extract the object pixels. As a consequence, the final result OD_f is obtained by using decision fusion of the detection results in three channels, OD_R, OD_G, and OD_B, as follows:

$$\mathrm{OD}_f = \mathrm{OD}_R \odot \mathrm{OD}_G \odot \mathrm{OD}_B \qquad (7)$$

where $\odot$ stands for the Hadamard product. That is, only the pixels detected by all channels are regarded as objects.

Postprocessing using an adaptive morphological opening operator is then applied on OD_f to remove noise and bridges in the linked platform. In this operator, the erosion operation can remove bridges and the following dilation operation can read the pixels on edges guaranteeing the accurate evaluation of the area size of offshore infrastructure. In the morphological opening operator, an adaptive structural element is proposed

$$d_i = \left\lfloor \left(\frac{La_i - L_{g\min}}{L_{g\max} - L_{g\min}} \times (w_2 - w_1 + 1) + w_1 \right) \times \frac{r_{s2}}{r_i} \right\rfloor \qquad (8)$$

where r_{s2} presents the spatial resolution of Sentinel-2 image, i.e., 10 m. $L_{g\max}$ and $L_{g\min}$ are the maximum and minimum lengths of the major axis in the obtained "guided area" of all detected objects. For the ith detected object, d_i is the radius value, r_i is the spatial resolution of the input image, and La_i stands for the length value of the major axis of its "guided area." The $[w_1, w_2]$ denotes the range of d_i and set to $[0, 1]$ in this article. In this way, the morphological opening is only operated on the linked platforms with large "guided area" sizes. This setting avoids the loss of blades in the detection of wind turbines.

From Fig. 6, it is clear that the linked platforms can be effectively extracted. The RGB fused morphological reconstruction method maintains the shape of the offshore infrastructure. As shown in Fig. 6(e), the adaptive postprocessing strategy successfully removed the bridges in linked platforms.

B. Size Estimation Model

In this section, based on the geolocation results, the topside area of oil/gas platforms and the diameter of the wind turbine are further determined for evaluation as follows.

1) Offshore Infrastructure Classification: First, wind turbines need to be separated from the oil/gas platforms and other targets before applying different kinds of measurement. To achieve this, here, two parameters, the minor axis and the circularity of the "guided area," are utilized

$$\mathrm{circularity} = \frac{4\pi \times Np}{P^2} \qquad (9)$$

where Np is the number of pixels in one detected object on Sentinel-2 data and P stands for the perimeter value. Wind turbines usually present a smaller topside area than almost all other kinds of offshore infrastructures. However, there are some small-sized infrastructures, such as the rig Mungo and Beryl Single Point Mooring (SPM)-3. Because of the long and slender
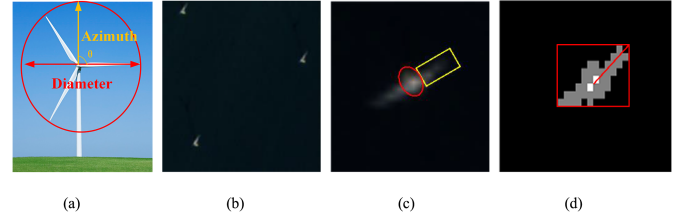
Fig. 7. Diameter length evaluation of wind turbines. (a) Wind turbines diagram. (b) True color Sentinel-2 image of three wind turbines in the Aberdeen Offshore Wind Farm. (c) Zoomed-in view of a single wind turbine with blade highlighted with yellow rectangular and nacelle marked with a red circle. (d) Detected wind turbine structure and bounding box settings.

blades, the wind turbines present a low circularity, whereas some semipermanent objects, such as FPSO, also have low circularity. Therefore, to separate the wind turbines from all oil/gas platforms and semipermanent objects, (10) is adopted. That is, for the ith detected object, if its minor axis of "guided area" is smaller than or equal to 10 and the circularity value is smaller than 1, then it is classified as a wind turbine

$$f(i) = \begin{cases} 1, & \text{if } Lo_i \leq 10 \text{ and circularity} < 1 \\ 0, & \text{otherwise} \end{cases} \qquad (10)$$

where Lo_i stands for the length value of the minor axis of its "guided area."

2) Determining the Topside Area of Oil/Gas Platforms: In the Sentinel-2 images, the topside area of the oil/gas platform, defined as the platform area above sea level, can be calculated based on the spatial resolution of the images. Given a spatial resolution of r_{S2} (meter), the topside area of one identified platform in the Sentinel-2 image is defined as follows:

$$S = Np \times r_{S2}^2 \qquad (11)$$

where S donates the topside area of one oil/gas platform.

3) Estimating the Diameter of Wind Turbines: The structures of slender blades and nacelle of the wind turbine can be observed in the Sentinel-2 image (see Fig. 7). As shown, the diameter can be calculated as twice the length of one blade. As shown in Fig. 7(a), θ is the rotational azimuth of one blade. When θ equals 90°, the full length of one blade is presented. Then, a bounding-box-based strategy is used to locate two blades of one wind turbine in the Sentinel-2 image.

A morphological erosion operation with a disc structural element, a radius of 1, is employed to erode the slender blades before detecting the center of nacelle parts. As shown in Fig. 7(d), the detected whole wind turbine is highlighted in gray, and the pixels of the nacelle center parts detected by the erosion operation are marked in white. By using the locations of nacelle pixels and the bounding box, the diameter of the wind turbine $Dist$ is calculated as twice the length of the longer blade

$$Dist = 2 \times \max \left(\sqrt{(x_{\mathrm{nac}} - x_1)^2 + (y_{\mathrm{nac}} - y_1)^2} , \right.$$

$$\left. \sqrt{(x_{\mathrm{nac}} - x_2)^2 + (y_{\mathrm{nac}} - y_2)^2} \right) \qquad (12)$$

where $(x_{\text{nac}}, y_{\text{nac}})$ is the center location of nacelle pixels; (x_1, y_1) and (x_2, y_2) denote locations of the top of two blades.

However, in most cases, the angular $\theta \neq 90°$. Consequently, only portions of the wind turbine blade are captured in the Sentinel-2 images as it keeps rotating. To improve the measurement accuracy, 12 consecutive images from Sentinel-2 time-series images are utilized. Specifically, the diameter is first calculated in each image, and the maximum in every four images is selected. The final diameter of one wind turbine is determined by averaging three maximum values.

C. Validation

A mask generated using the Scottish EEZ, the Scotland coastline, and baseline is utilized to exclude the land and island areas. The performance of the proposed method is quantitatively assessed in terms of the accuracy of the geolocation and size measurement of the offshore infrastructures within the whole study area. The ground truth constructed in Section II-B, including the latitude, longitude, and size for each offshore infrastructure, is given in Supplementary Material (see Tables S1–S6).

For quantitative evaluation of the geolocation of the offshore energy infrastructures, the detection probability (DP), overall accuracy (OA), commission rate (CR), and omission rate (OR) are employed. As illustrated in Supplementary Material (see Fig. S3), the ground truth only provides an approximate location of the target infrastructure, which is not situated at the exact center of the target. Therefore, the proposed method extracts all pixels that belong to each detected infrastructure to form a location range as the detection outcome. If the detected location range contains the positioned ground truth point, it is considered a correct detection. Otherwise, if a detected location range does not encompass any positioned ground truth point, it can be deemed as a commission error, i.e., false detection. This occurrence arises because of the misidentification of other objects as offshore energy infrastructures. In the case that no location range is detected for a positioned ground truth point, it is regarded as an omission by the proposed method.

The DP, OA, CR, and OR are calculated as follows, where *Na, NG, Nc,* and *No* denote, respectively, the number of offshore energy infrastructures that is correctly detected, the actual total number of offshore energy infrastructures in the ground truth data, the number of the objects that is misidentified as the offshore energy infrastructures, and the number of offshore energy infrastructures that is omitted by the proposed method.

$$\text{DP} = Na / (NG \times 100\%) \tag{13}$$

$$\text{CR} = Nc / (NG \times 100\%) \tag{14}$$

$$\text{OR} = No / (NG \times 100\%) \tag{15}$$

$$\text{OA} = Na / ((Na + Nc + No) \times 100\%). \tag{16}$$

The comparison analysis was conducted and benchmarked with two state-of-the-art offshore energy infrastructure detection methods. The first is the GEE offshore infrastructure detector (GEEOID), using the Sentinel-1 SAR data [6]. GEEOID used the median-filtered composite strategy, a difference of Gaussians, and postprocessing operations of erosion and dilation. The offshore infrastructure map capability of GEEOID has

been validated through the detection of the oil platforms in the Gulf of Mexico and the extraction of the wind turbines in the waters of China and the United Kingdom. In this study, the prior testing of parameter settings is carried out in the Scottish waters. The optimal configurations encompassed 50 m in erosion, 5 m in dilation, and a threshold value set at 0.85. For analysis, the Sentinel-1 data from June 2020 to January 2022 are adopted. The second compared method is the NDWI composite method [16] based on the optical imagery, which includes the minimum NDWI (Min_NDWI), maximum NDWI (Max_NDWI), and mean NDWI (Mean_NDWI). It uses the Landsat-7 ETM+ images in two consecutive years in the Caspian Sea for identification and Night-light data and Sentinel-2 images for verification. Different thresholds are applied on the NDWI composite to classify the water, island, and offshore oil/gas platforms with certain rules: water body (Max_NDWI>0.55), island (Min_NDWI<−0.05), and offshore oil/gas platforms (0<Mean_NDWI<0.4). Herein, we apply the NDWI composite method to the Scottish waters to investigate its performance. To ensure a comprehensive coverage of the entire study area in the Scottish waters, this study utilizes data from Landsat 7, Landsat 8, and Sentinel-2 for two consecutive years, i.e., from June 2020 to July 2022. The optimal threshold value for oil/gas platform extraction is set to 0.3 after trail tests in the study area.

For evaluating the size detection accuracy, the size error (SE) and mean size error (MSE) are utilized. Here, SE indicates the difference between the extracted size and the actual size of each infrastructure in the ground truth, and MSE denotes the average SE value for all the extracted offshore infrastructures. Considering the varying sizes of different offshore infrastructures, the size error rate (SER) is also computed as the ratio of SE and the actual size of each offshore energy infrastructure as well as the mean size error rate (MSER), which refers to the average SER for all the detected infrastructures.

The proposed method is implemented using the MATLAB 2018a platform on a computer with an Intel Core i7-8700 CPU (3.20 GHz) and 16.0 GB of memory.

IV. RESULTS

A. Geolocation Accuracy Analysis

1) Quantitative Evaluation of the Geolocation Accuracy: In Scottish waters, a diverse range of offshore energy infrastructure can be found, including oil/gas platforms, semipermanent objects, and wind turbines. Table I provides a summary of their respective quantities. By combining the Sentinel-1 SAR data and Sentinel-2 MSI data, our method can correctly detect 332 objects only with one omission. The one omission is from the bridge-linked platforms, i.e., BERYL FLARE. Thus, for all offshore infrastructures in Scottish waters, the probability of detection and OA is 99.70% and the commission error rate is 0%. Specifically, the DP is 100% for offshore wind turbines, single oil/gas platforms, and semipermanent objects. The DP for bridge-linked platforms is 97.92%. More discussions are given in Section V. Fig. 8 illustrates the spatial distribution of the detection results, while the detected location range is detailed in Supplementary Material (see Tables S7–S12).

This article has been accepted for inclusion in a future issue of this journal.

IEEE JOURNAL OF OCEANIC ENGINEERING
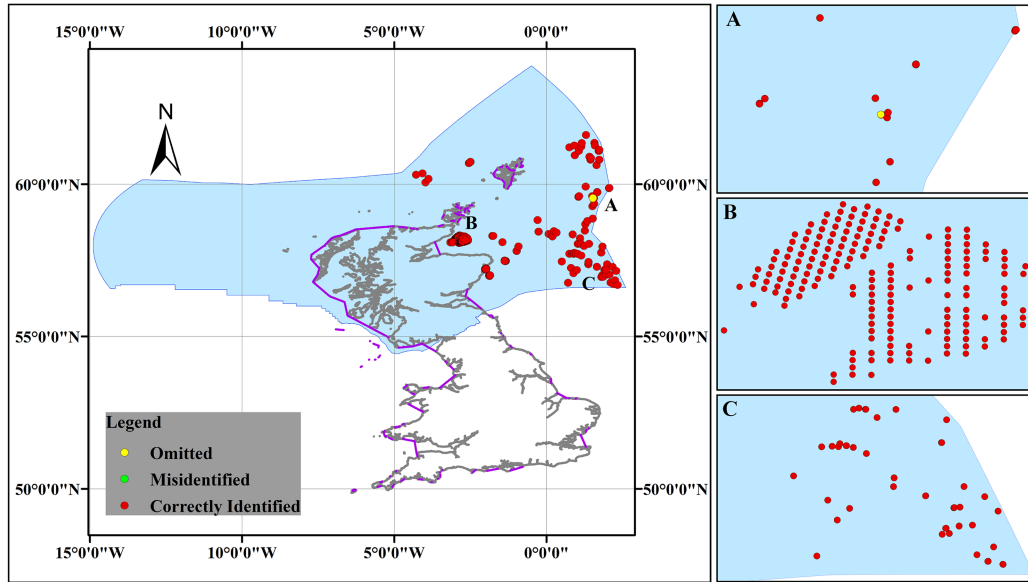
Fig. 8.   Offshore infrastructure detection results by our proposed method.

TABLE I
NUMBER OF DIFFERENT OFFSHORE INFRASTRUCTURES IN THE GROUND TRUTH

Offshore Infrastructure	Categories	Number
Oil/gas Platform	Single	54
	Bridge-linked	48
Wind Farm	Beatrice	86 wind turbines and 2 OTMs
	Moray East	100 wind turbines and 3 OSPs
	HyWind	5 wind turbines
	Kincardine	5 wind turbines
	Aberdeen	11 wind turbines
Semipermanent objects	-	19

TABLE II
DETECTION RESULTS OF DIFFERENT METHODS ON 333 OFFSHORE
INFRASTRUCTURES IN SCOTTISH WATERS

Metrics	The proposed method	GEEOID	NDWI composite
Correct Identification	332	324	300
Commission	0	5	11
Omission	1	9	33
Commission rate	0%	1.50%	3.20%
Omission rate	0.30%	2.70%	9.90%
Overall accuracy	99.70%	95.86%	87.20%

As shown in Fig. 8, the correctly identified offshore infrastructures are marked as red dots and omissions are highlighted as yellow dots. The zoomed-in images for area A show the detection in the east part of the EEZ, from which we can find the distribution of the omitted structure. The zoomed-in image for area B presents the wind turbines distribution in the Beatrice Offshore Wind Farm and Moray East Offshore Wind Farm. As seen in Fig. 8, most offshore infrastructures are located in the eastern waters of Scotland. This intensive distribution results in more background noise and moving vessels.

2) Comparison With Other Methods: The comparison results are given in Table II. With an OA of 95.86%, the GEEOID method can successfully detect 324 out of 333 offshore infrastructures in Scottish waters. Specifically, all the wind turbines are successfully identified with a DP of 100%. In comparison with the proposed method, GEEOID generates several omissions that primarily arise from linked oil/gas platforms with intricate structures. The original literature of GEEOID [6] states that

these linked oil/gas platforms are considered as a single infrastructure, without attempting to differentiate the individual rigs within each linked oil/gas platform. Consequently, the coarse resolution of Sentinel-1 data utilized by GEEOID fails to provide sufficient detailed information for accurate identification and differentiation.

As given in Table II, the NDWI composite method generates an overall detection accuracy of 87.20%. Compared with the other two methods, the NDWI composite produces more omissions, which are mainly from the wind farm areas and linked oil/gas platforms. The offshore infrastructure detection in Scottish waters is more complicated because there are different kinds of infrastructures, including oil/gas platforms, wind turbines, semipermanent objects, and so on. The frequent cloud coverage on optical data and the fixed threshold value settings have led to difficulties in detecting small-sized wind turbines. Although clouds and shadow removal algorithms are employed to reduce the influence on the NDWI index, many noise objects still remain and result in misidentifications.

B. Evaluation of the Estimated Size Accuracy

1) Size Accuracy of the Topside of Oil/Gas Platforms and Semipermanent Objects: The calculated topside area of all

TABLE III
CORRESPONDING NUMBER OF INFRASTRUCTURE WITH DIFFERENT SE AND MSE

Categories	Oil/gas platform	Semipermanent object
SE < 100 m^2	20	5
SE < 300 m^2	55	7
SE < 500 m^2	82	9
Total Number	89	19
MSE	45.5	765.9

TABLE IV
NUMBER OF INFRASTRUCTURE WITH DIFFERENT SER AND THE CORRESPONDING MSER

Categories	Oil/gas platform	Semipermanent object
SER < 1%	8	5
SER < 10%	63	12
SER < 20%	82	15
Total Number	89	19
MSER	7.64%	12.56%

correctly identified oil/gas platforms and semipermanent infrastructure are listed in Supplementary Material (see Table S13), where the size evaluation accuracies are summarized in Tables III and IV for comparison. With a spatial resolution of 10 m, the area size of the corresponding surface for 1 pixel is 100 m^2. As illustrated in these tables, our proposed strategies for evaluating the topside area have achieved promising results. For the 19 semipermanent objects and 101 oil/gas platforms detected by our method, there are 12 rigs, i.e., Ninian North, Northern Producer, Brent Bravo, Brent Delta, Beatrice Charlie, Beatrice Alpha Drilling, Beatrice Alpha Production, Beatrice Bravo, Manifold and Compression Platform 01, Frigg Treatment platform 1, Frigg Concrete drilling platform 1, and Frigg Treatment Compression Platform 2, have undergone decommissioning in recent years with many structures being removed or partially removed. For these decommissioning structures, accurate detection of cut legs above the water is of minor importance in documenting offshore energy infrastructure, as this is a temporary state during the decommissioning process. Final decommissioning in the North Sea requires that all platforms are either fully removed or cut to footing below the sea surface with no surface elements remaining. To this end, we exclude such objects in size evaluation in this article. As a result, the topside sizes of 89 oil/gas platforms and 19 semipermanent objects are evaluated.

As given in Table III, for 20 out of 89 rigs (or 22.473%), the SE is lower than 100 m^2, i.e., less than 1 pixel in Sentinel-2 images. For 55 oil/gas platforms (or 61.80%), the SE is lower than 300 m^2, i.e., 3 pixels. On the other hand, more than 5 pixels

SE is generated on seven rigs, namely, Cormorant A, Eider, Piper B, Brae A, Golden Eagle Wellhead Platform, Golden Eagle PUQ Platform, and Elgin PUQ. The linked platforms usually exhibit a large contour range in the Sentinel-1 data, which leads to a high radius value setting of structural elements in morphological opening operation. However, the rigs in linked structures usually have different topside area sizes. The smaller rig in the linked platforms will be recognized as a smaller size than its actual area. Overall, the MSE on the oil/gas platforms is 45.5 m^2, i.e., less than 1 pixel in Sentinel-2 images, which has validated the effectiveness of our proposed method. With regard to the SER given in Table IV, there are 8 infrastructures (or 8.99%) with an SER lower than 1%, while 63 structures (or 70.79%) have an SER smaller than 10%. On 7 infrastructures (or 7.87%), the SER is larger than 20%, which includes Beryl Alpha, Beryl SPM-3, Bruce D, Golden Eagle Wellhead Platform, Forties Unity, Cats Riser, and Elgin PUQ. These infrastructures have relatively small topside area sizes. Thus, even if they show a small SE around 3 pixels in the Sentinel-2 image, the SERs are still high and further increase the MSER. On the contrary, there are infrastructures, such as Cormorant A, Piper B, and Brae A, that show high SEs but low SERs. This is mainly because they have large actual topside area sizes. These results further validate the challenges of estimating the size of linked rigs. More details on the infrastructure with large SE and SER are discussed in Section V.

As for the topside area estimation of semipermanent objects, 5 out of 19 (or 26.32%) have achieved an SE lower than 1 pixel in the Sentinel-2 images, while 7 out of 19 (or 36.84%) obtain an error lower than 300 m^2, or 3 pixels in the Sentinel-2 image. There are 9 objects (or 47.37%) that are detected with an SE higher than 500 m^2, or 5 pixels in the Sentinel-2 image. In contrast to the oil/gas platforms with a fixed location, the semipermanent objects would drift with waves. In the Sentinel-1 time-series images, only the parts of semipermanent objects with high repetition are detected. Therefore, the detected contour range in the Sentinel-1 is too small to extract the whole size of these objects in the Sentinel-2 images. The obtained MSE becomes 765.9 m^2 (or around 8 pixels in the Sentinel-2 image), which is higher than that of oil/gas platforms. Similarly, these semipermanent structures present a high MSER of 12.56%, as given in Table IV. Here, four objects (or 21.05%) have an SER higher than 20%, including Kraken FPSO, Alba FPSO, Pierce FPSO, and Culzean FPSO. Our method only detects their partial structures because of the limited contour range. They also have a higher SE than 20 pixels in the Sentinel-2 image, which significantly increases the MSE and MSER results for semipermanent objects. However, the other 12 (or 63.16%) semipermanent objects show a lower SER than 10%. That is, most semipermanent objects can achieve promising SER results.

2) Accuracy of Estimated Diameter of the Wind Turbines: The accuracy of the estimated diameters of the wind turbines is evaluated in this section. Due to a low spatial resolution of 10 m, the calculated length which is less than 1 pixel is presented as ±5 m. Table V summarizes the evaluation results of the estimated diameters for the wind turbines, where the detailed detected results from all wind farms are given in Supplementary Material (see Tables S14–S18). The actual diameters in different

This article has been accepted for inclusion in a future issue of this journal.

IEEE JOURNAL OF OCEANIC ENGINEERING

TABLE V
DIAMETER LENGTH EVALUATION OF WIND TURBINES IN SCOTTISH WATERS

Name (Numbers)	True Length (m)	SE≤5±5 m	SE≤10±5 m	SE≤20±5 m	SE≤30±5 m	MSE (MSER)
Beatrice (86)	154	22	55	86	86	9.3 ± 5 m (6.04%)
Moray East (100)	164	10	59	94	100	10.6±5 m (6.46%)
HyWind (5)	154	2	5	5	5	5.8 ± 5 m (3.77%)
Kincardine (5)	164	2	5	5	5	6.4 ± 5 m (3.90%)
Aberdeen (11)	150	8	11	11	11	6.4 ± 5 m (4.27%)
Summary (207)	-	44	135	201	207	7.7 ± 5 m (4.89%)

wind farms vary in the Scottish waters, which are listed in Table V.

In the Beatrice Offshore Wind Farm, there are 86 wind turbines apart from the 2 offshore transformer modules (OTMs). Among them, the SE of the estimated diameters for 22 wind turbines (or 25.58%) is less than 5 ± 5 m (SER<3.25%). For 55 wind turbines, the errors are lower than 10 ± 5 m (SER<6.49%). In addition, the SE of all wind turbines in the Beatrice Offshore Wind Farm is lower than 20 ± 5 m (SER<12.99%), i.e., 2 pixels in the Sentinel-2 images. Overall, the MSE of wind turbines in the Beatrice Offshore Wind Farm is 9.3 ± 5 m (MSER is 6.04%), which is around 1 pixel in the Sentinel-2 images. In Moray East Offshore Wind Farm, there are 100 wind turbines and 3 offshore substation platforms (OSPs), in which 10 out of 100 wind turbines (or 10%) have an SE lower than 55 ± 5 m (SER<3.05%). There are 59 wind turbines (or 59%) with an SE lower than 10 ± 5 m (SER<6.10%) and 94 wind turbines with an SE lower than 20 ± 5 m (SER<12.20%). No wind turbine is estimated with an SE larger than 30 ± 5 m. The MSE is around 1 pixel in the Sentinel-2 image. In the HyWind, Kincardine, and Aberdeen Offshore Wind farms, all wind turbines show SE lower than 10 ± 5 m. The MSE and MSER in the HyWind, Kincardine and Aberdeen Offshore Wind farms are all less than 10 m (1 pixel in the Sentinel-2 image) and 5%, respectively.

In summary, there are 207 wind turbines in the study area, of which 135 (65.21%) of them have an SE lower than 10 ± 5 m. The 201 (97.10%) wind turbines show an SE lower than 20 ± 5 m, i.e., 2 pixels in the Sentinel-2 image. The MSE and MSER for wind turbines in the whole of Scottish waters are 7.7 ± 5 m and 4.89%, respectively. For the different offshore wind farms in Scottish waters, the MSE is all less than 20 ± 5 m and the MSER is lower than 7%. These results further validate the effectiveness of our proposed method in the size evaluation of offshore infrastructures. It provides the potential for monitoring and analyzing the wind turbine blades in the future.

V. DISCUSSIONS

Fig. 9(a) and (b) shows the cases of omissions in the location detection and infrastructures with a large SE in the Sentinel-1 and the final detection results in Fig. 9(c). For the location detection, there is one omission which is from the platform
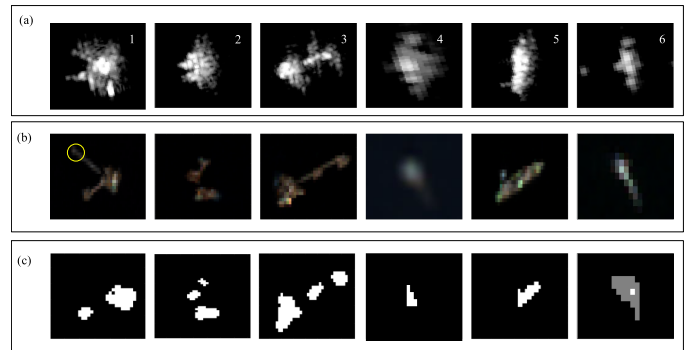
Fig. 9. Different kinds of offshore infrastructure in (a) Sentinel-1, (b) Sentinel-2, and (c) detection results.

complex, i.e., linked oil/gas platforms with bridges. As shown in Fig. 9(b), our method fails to identify the platform Beryl flare in infrastructure #1 (marked in yellow circles). This omission is because the platform Beryl flare shows similar spectral and spatial features with the bridges (e.g., color, size, and shape). This case is more complex. The structural element in morphological opening operation can identify the pixels and the corresponding neighborhood in the image to be processed [50]. This platform is identified as the part of bridge and then removed by the morphological opening operation. For infrastructures #2 and #3, the high SE and SER are generated. These are mainly because the same radius values of structural elements in morphological operators are used for all rigs in one linked structure, even though rigs show different topside area sizes. Infrastructure #2 consists of platforms Bruce PUQ, Bruce CR, and Bruce D, where the platforms Bruce CR and Bruce D are identified with higher SER than 10%. The platform Elgin PUQ in infrastructure #3 is identified with SE equaling around 9 pixels in the Sentinel-2 image. It is clear from Fig. 9(b) that in infrastructures #2 and #3, rigs have significantly different topside area sizes. Infrastructure #4 is the Beryl SPM-3, which has a significantly smaller size than the oil/gas platform. Because of the small size, weak intensity, and 2D-SSA filter used in the proposed method, the detected contour range is limited in the Sentinel-1 data. As shown in Fig. 9(c), based on the "guided area" obtained from the Sentinel-1 data, only part of the structure is detected and evaluated in the Sentinel-2 image. As a result, the structure is

detected with a large SER. In contrast to the fixed position of the oil/gas platform and wind turbine, most semipermanent objects are floating steel, which makes them easily drift with waves. After the temporal median operation, only the area with a high appearance frequency of these floating objects can be detected as the contour range, which inevitably narrows the "guided area" in the Sentinel-2 images. The detection result of infrastructure #5, namely, Pierce FPSO, is illustrated in Fig. 9. By comparing Fig. 9(a) and (b), it is clear that this FPSO has shifted slightly over time. As a result, only a small part is extracted, as shown in Fig. 9(c), which significantly increases the SE evaluation. Infrastructure #6 is the wind turbine BE-G12 in the Beatrice Offshore Wind Farm. As shown, the proposed method fails to extract the nacelle part correctly, which leads to the error in the blade length estimate and finally obtains a short diameter size. For most wind turbines, the generated SE is mainly because of the inaccurately detected location of nacelle parts.

VI. CONCLUSION

In this article, we have proposed an automatic method for geolocating and measuring of offshore energy infrastructure by leveraging multimodal satellite data, i.e., Sentinel-1 SAR and Sentinel-2 MSI data. First, we demonstrate that by using the complementary strengths of SAR and MSI data, our method can produce highly accurate geolocation of the offshore energy infrastructure in Scottish waters, specifically diverse rigs within interconnected oil/gas platforms. With a remarkable detection accuracy of 99.70% achieved for 333 offshore infrastructures, our method has successfully extracted all single oil/gas platforms, wind turbines, and nearly all rigs within linked oil/gas platforms with only a single omission observed. Second, the proposed classification model, which utilizes the minor axis and circularity of the "guided area," has proven to be very effective in distinguishing wind turbines from other offshore energy infrastructure. As a result, the model enables automated size measurements, allowing for independent measurement of the topside area size of oil/gas platforms and semipermanent objects, as well as the diameter length of wind turbines. The SEs for wind turbines, oil/gas platforms, and semipermanent objects are around 1, 1, and 8 pixels, respectively, in the Sentinel-2 images, while the SER is less than 10% for most of the structures. To sum up, our proposed method has realized automatic geolocation and size measurement of different kinds of offshore energy infrastructure. The experimental results have demonstrated its efficacy in automatic offshore infrastructure detection and evaluation in a vast sea area, which has met the needs for practical applications. The future work will expand upon the research in self-attention modeling [51], rapid and cost-effective object detection [52], change detection, and monitoring of offshore energy infrastructure [53], [54].

REFERENCES

[1] P. E. Posen et al., "Evaluating differences in marine spatial data resolution and robustness: A North Sea case study," *Ocean Coastal Manage.*, vol. 192, 2020, Art. no. 105206.

[2] B. J. Williamson et al., "A self-contained subsea platform for acoustic monitoring of the environment around marine renewable energy devices–field deployments at wave and tidal energy sites in Orkney, Scotland," *IEEE J. Ocean. Eng.*, vol. 41, no. 1, pp. 67–81, Jan. 2016.

[3] T. Zhang et al., "Global offshore wind turbine dataset," *Sci. Data*, vol. 8, 2021, Art. no. 191.

[4] V. Parente et al., "Offshore decommissioning issues: Deductibility and transferability," *Energy Policy*, vol. 34, pp. 1992–2001, 2006.

[5] Y. Wang and H. Liu, "A hierarchical ship detection scheme for high-resolution SAR images," *IEEE Trans. Geosci. Remote Sens.*, vol. 50, no. 10, pp. 4173–4184, Oct. 2012.

[6] B. A. Wong, C. Thomas, and P. Halpin, "Automating offshore infrastructure extractions using synthetic aperture radar and Google Earth Engine," *Remote Sens. Environ.*, vol. 233, 2019, Art. no. 111412.

[7] Y. Liu et al., "Automatic extraction of offshore platforms using time-series Landsat-8 operational land imager data," *Remote Sens. Environ.*, vol. 175, pp. 73–91, 2016.

[8] J. Li et al., "Deep learning in multimodal remote sensing data fusion: A comprehensive review," *Int. J. Appl. Earth Observ. Geoinf.*, vol. 112, 2022, Art. no. 102926.

[9] G. Benassai, D. D. Luccio, V. Corcione, F. Nunziata, and M. Migliaccio, "Marine spatial planning using high-resolution synthetic aperture radar measurements," *IEEE J. Ocean. Eng.*, vol. 43, no. 3, pp. 586–594, Jul. 2018.

[10] W. Gao et al., "Monitoring terrain elevation of intertidal wetlands by utilising the spatial-temporal fusion of multi-source satellite data: A case study in the Yangtze (Changjiang) Estuary," *Geomorphology*, vol. 383, 2021, Art. no. 107683.

[11] Q. Zhao et al., "An overview of the applications of earth observation satellite data: Impacts and future trends," *Remote Sens.*, vol. 14, 2022, Art. no. 1863.

[12] P. Ma et al., "Multiscale superpixelwise prophet model for noise-robust feature extraction in hyperspectral images," *IEEE Trans. Geosci. Remote Sens.*, vol. 61, 2023, Art. no. 5508912.

[13] S. Zhao et al., "Extraction and monitoring of offshore oil and gas platforms based on Landsat imagery," *Trop. Geography*, vol. 37, pp. 112–119, 2017.

[14] Z. Zhu, Y. Tang, and T. Han, "Offshore platform detection based on Harris detector and intensity-texture image from Sentinel_2A image," in *Proc. 10th Int. Assoc. Pattern Recognit. Workshop Pattern Recognit. Remote Sens.*, 2018, pp. 1–4.

[15] W. Xu et al., "Proliferation of offshore wind farms in the North Sea and surrounding waters revealed by satellite image time series," *Renewable Sustain. Energy Rev.*, vol. 133, 2020, Art. no. 110167.

[16] H. Zhu et al., "Detecting offshore drilling rigs with multitemporal NDWI: A case study in the Caspian Sea," *Remote Sens.*, vol. 13, 2021, Art. no. 1576.

[17] T. A. Croft, "Nighttime images of the Earth from space," *Sci. Amer.*, vol. 239, pp. 86–101, 1978.

[18] S. Casadio, O. Arino, and A. Minchella, "Use of ATSR and SAR measurements for the monitoring and characterisation of night-time gas flaring from off-shore platforms: The North Sea test case," *Remote Sens. Environ.*, vol. 123, pp. 175–186, 2012.

[19] O. C. Anejionu, G. A. Blackburn, and J. D. Whyatt, "Detecting gas flares and estimating flaring volumes at individual flow stations using MODIS data," *Remote Sens. Environ.*, vol. 158, pp. 81–94, 2015.

[20] C. D. Elvidge et al., "Methods for global survey of natural gas flaring from visible infrared imaging radiometer suite data," *Energies*, vol. 9, 2015, Art. no. 14.

[21] C. D. Elvidge et al., "VIIRS nightfire: Satellite pyrometry at night," *Remote Sens.*, vol. 5, pp. 4423–4449, 2013.

[22] L. Cheng et al., "Invariant triangle-based stationary oil platform detection from multitemporal synthetic aperture radar data," *J. Appl. Remote Sens.*, vol. 7, 2013, Art. no. 073537.

[23] W. An, M. Lin, and H. Yang, "Stationary marine target detection with time-series SAR imagery," *IEEE J. Sel. Topics Appl. Earth Observ. Remote Sens.*, vol. 14, pp. 6406–6413, 2021.

[24] F. Nunziata and M. Migliaccio, "On the COSMO-SkyMed PingPong mode to observe metallic targets at sea," *IEEE J. Ocean. Eng.*, vol. 38, no. 1, pp. 71–79, Jan. 2013.

[25] Z. Xu et al., "Dynamic detection of offshore wind turbines by spatial machine learning from spaceborne synthetic aperture radar imagery," *J. King Saud Univ.-Comput. Inf. Sci.*, vol. 34, pp. 1674–1686, 2022.

[26] Y. Liu et al., "Assessment of offshore oil/gas platform status in the northern Gulf of Mexico using multi-source satellite time-series images," *Remote Sens. Environ.*, vol. 208, pp. 63–81, 2018.

This article has been accepted for inclusion in a future issue of this journal.

IEEE JOURNAL OF OCEANIC ENGINEERING

[27] A. Marino, D. Velotto, and F. Nunziata, "Offshore metallic platforms observation using dual-polarimetric TS-X/TD-X satellite imagery: A case study in the Gulf of Mexico," *IEEE J. Sel. Topics Appl. Earth Observ. Remote Sens.*, vol. 10, no. 10, pp. 4376–4386, Oct. 2017.

[28] Y. Liu et al., "Geometric accuracy of remote sensing images over oceans: The use of global offshore platforms," *Remote Sens. Environ.*, vol. 222, pp. 244–266, 2019.

[29] T. Hoeser, S. Feuerstein, and C. Kuenzer, "DeepOWT: A global offshore wind turbine data set derived with deep learning from Sentinel-1 data," *Earth Syst. Sci. Data*, vol. 14, pp. 4251–4270, 2022.

[30] United Kingdom Hydrographic Office, "Scottish Zone (200M limit) - exclusive economic zone (EEZ) adjacent to Scotland - exclusive economic zone (EEZ) order 2013," 2013, Accessed: Dec. 31, 2021. [Online]. Available: https://marine.gov.scot/maps/416

[31] European Marine Observation and Data Network, "The Scotland coastline," 2020, Accessed: Jan. 15, 2022. [Online]. Available: https://www.emodnet-bathymetry.eu/media/emodnet_bathymetry/org/documents/emodnet_coastline_and_baseline_collection_2020-18dec2020.pdf

[32] OSPAR Commission, "OSPAR inventory of offshore installations - 2019," 2019, Accessed: Dec. 31, 2021. [Online]. Available: https://odims.ospar.org/en/submissions/ospar_offshore_installations_2019_01/

[33] Oil and Gas Authority, "Offshore oil and gas activity," 2021, Accessed: Jan. 4, 2022. [Online]. Available: https://ogauthority.maps.arcgis.com/apps/webappviewer/index.html?id=adbe5a796f5c41c68fc762ea137a682e

[34] European Space Agency, "EO browser," 2017, Accessed: Jan. 4, 2022. [Online]. Available: https://www.sentinel-hub.com/explore/eobrowser/

[35] Marine Scotland, "Beatrice Offshore Wind Farm consent plan," 2015, Accessed: Jan. 2, 2022. [Online]. Available: https://marine.gov.scot/sites/default/files/00510248.pdf

[36] Marine Scotland, "Development layout and specification plan — Moray East Offshore Wind Farm and associated offshore transmission infrastructure," 2018, Accessed: Jan. 15, 2022. [Online]. Available: https://marine.gov.scot/sites/default/files/moray_east_dslp_version_2_final_aug_2018.pdf

[37] Marine Scotland, "The design statement for Aberdeen Offshore Wind Farm," 2017, Accessed: Jan. 15, 2022. [Online]. Available: https://marine.gov.scot/sites/default/files/00518408.pdf

[38] Marine Scotland, "Hywind Scotland pilot park project plan for construction activities," 2017, Accessed: Feb. 7, 2022. [Online]. Available: https://marine.gov.scot/sites/default/files/00516548_0.pdf

[39] Marine Scotland, "Kincardine offshore windfarm - development specification and layout plan," 2023, Accessed: Jul. 10, 2023. [Online]. Available: https://marine.gov.scot/data/kincardine-offshore-windfarm-development-specification-and-layout-plan-dslp

[40] European Space Agency, "Revisit and coverage," 2021, Accessed: Sep. 10, 2023. [Online]. Available: https://sentinels.copernicus.eu/web/sentinel/user-guides/sentinel-1-sar/revisit-and-coverage

[41] European Space Agency, "Mission ends for Copernicus Sentinel-1B satellite," 2022, Accessed: Sep. 10, 2023. [Online]. Available: https://www.esa.int/Applications/Observing_the_Earth/Copernicus/Sentinel-1/Mission_ends_for_Copernicus_Sentinel-1B_satellite

[42] G. V. Weinberg, "General transformation approach for constant false alarm rate detector development," *Digit. Signal Process.*, vol. 30, pp. 15–26, 2014.

[43] J. Zabalza et al., "Novel two-dimensional singular spectrum analysis for effective feature extraction and data classification in hyperspectral imaging," *IEEE Trans. Geosci. Remote Sens.*, vol. 53, no. 8, pp. 4418–4433, Aug. 2015.

[44] P. Ma, J. Ren, H. Zhao, G. Sun, P. Murray, and J. Zheng, "Multiscale 2-D singular spectrum analysis and principal component analysis for spatial–spectral noise-robust feature extraction and classification of hyperspectral images," *IEEE J. Sel. Topics Appl. Earth Observ. Remote Sens.*, vol. 14, pp. 1233–1245, 2021.

[45] H. Fu, G. Sun, A. Zhang, B. Shao, J. Ren, and X. Jia, "Tensor singular spectral analysis for 3D feature extraction in hyperspectral images," *IEEE Trans. Geosci. Remote Sens.*, vol. 61, 2023, Art. no. 5403914.

[46] N. Otsu, "A thresholding selection method from gray-level histogram," *IEEE Trans. Syst., Man, Cybern.*, vol. 9, no. 1, pp. 62–66, Jan. 1979.

[47] E. Grosso and R. Guida, "A new automated ship wake detector for small and go-fast ships in Sentinel-1 imagery," *Remote Sens.*, vol. 14, 2022, Art. no. 6223.

[48] X. Luo, X. Tong, and H. Pan, "Integrating multiresolution and multitemporal Sentinel-2 imagery for land-cover mapping in the Xiongan new area, China," *IEEE Trans. Geosci. Remote Sens.*, vol. 59, no. 2, pp. 1029–1040, Feb. 2021.

[49] B. Han, "Watershed segmentation algorithm based on morphological gradient reconstruction," in *Proc. 2nd Int. Conf. Inf. Sci. Control Eng.*, 2015, pp. 533–536.

[50] J. Serra, "Mathematical morphology," in *Encyclopedia of Mathematical Geosciences*. Berlin, Germany: Springer-Verlag, 2022, pp. 1–16.

[51] G. Xie et al., "Self-attention enhanced deep residual network for spatial image steganalysis," *Digit. Signal Process.*, vol. 139, 2023, Art. no. 104063.

[52] R. Chen et al., "Rapid detection of multi-QR codes based on multistage stepwise discrimination and a compressed MobileNet," *IEEE Internet Things J.*, vol. 10, no. 18, pp. 15966–15979, Sep. 2023.

[53] Y. Li et al., "CBANet: An end-to-end cross band 2-D attention network for hyperspectral change detection in remote sensing," *IEEE Trans. Geosci. Remote Sens.*, vol. 61, 2023, Art. no. 5513011.

[54] F. Luo, T. Zhou, J. Liu, T. Guo, X. Gong, and J. Ren, "Multiscale diff-changed feature fusion network for hyperspectral image change detection," *IEEE Trans. Geosci. Remote Sens.*, vol. 61, 2023, Art. no. 5502713.

Ping Ma received the Ph.D. degree in signal processing with the Department of Electronic and Electrical Engineering, University of Strathclyde, Glasgow, U.K., in 2022.

She is currently a Research Fellow with the National Subsea Centre, Robert Gordon University, Aberdeen, U.K. Her research is primarily focused on multimodal remote sensing, hyperspectral imaging, and machine learning.

Malcolm Macdonald received the Ph.D. degree in astrodynamics from the University of Glasgow, Glasgow, U.K., in 2002.

He currently serves as the Director of the Centre for Signal and Image Processing (CeSIP) and holds the position of Director with the Applied Space Technology Laboratory, a part of CeSIP, University of Strathclyde, Glasgow, U.K. His research is primarily focused on a wide range of areas within the field of space technology, including space mission analysis and design, astrodynamics, swarm engineering, network systems, and systems engineering.

Sally Rouse received the Ph.D. degree in artificial reef ecology from the University of Aberdeen, Aberdeen, U.K., in 2016.

She currently holds the position of Offshore Energy Environmental Advice Group Leader at Marine Scotland Science, Aberdeen, U.K. Her expertise lies in the study and consultation regarding the marine environmental consequences associated with the installation and decommissioning of offshore oil and gas infrastructure. Her research interests are centered on various crucial aspects, including the intersection of commercial fisheries with the oil and gas industry, the effects of oil and gas extraction on benthic ecosystems, and the field of artificial reef ecology.

Jinchang Ren (Senior Member, IEEE) received the Ph.D. degree in electronic imaging from the University of Bradford, Bradford, U.K., in 2009.

He is currently a Professor of Computing Science with Robert Gordon University, Aberdeen, U.K. He is the Lead of the Transparent Ocean Group and Director of the Hyperspectrall Inaging Lab, National Subsea Centre, working on multimodal sensing based inspection and condition monitoring of marine/energy infrastructures and ocean environments. His research interests include hyperspectral imaging, image processing, computer vision, big data analytics, and machine learning.